Nyquist-compliant cycloidal computed tomography

G. Lioliou,[1] A. Charman,[2] O. Roche i Morgó,[1] M. Endrizzi,[1] S. Arridge,[3] D. Bate,[2] A. Olivo,[1] and C. Hagen[1,*]

[1] *Department of Medical Physics and Biomedical Engineering, University College London, London, United Kingdom*

[2] *Nikon X-Tek Systems Ltd, Tring Business Centre, Tring, United Kingdom*

[3] *Department of Computer Science, University College London, London, United Kingdom*

(Received 14 May 2024; accepted 16 August 2024; published 4 September 2024)

Cycloidal computed tomography, by which a lateral sample translation and rotation are combined, is a fully-fly-scan-compatible acquisition scheme for micro-computed-tomography systems using amplitude-modulated beams. Such systems have gained popularity, as they enable x-ray phase-contrast imaging (XPCI) and aperture-driven spatial resolution. The former provides superior contrast for weakly attenuating samples, while the latter allows the resolution of a micro-computed-tomography system to be increased beyond the conventional limit dictated by the source and detector. Such systems initially required time-inefficient step-and-shoot acquisitions, a limitation that has been removed by the development of cycloidal computed tomography. Here we derive cycloidal sampling conditions that are optimal in the sense of the Nyquist-Shannon theorem. Their availability enables the acquisition of well-sampled (i.e., high-resolution) XPCI images in a time-efficient manner, a long-sought outcome with relevance to laboratory implementations, where scan times have traditionally been long, and to synchrotron implementations, where the next frontier is to achieve high-speed (e.g., dynamic) imaging. We make no assumptions on the type of x-ray source used, but demonstrate the optimal conditions with a rotating-anode x-ray tube.

DOI: 10.1103/PhysRevApplied.22.034011

I. INTRODUCTION

X-ray micro-computed-tomography (micro-CT), a technology available with laboratory x-ray sources and at synchrotrons, allows the scanning of centimeter-scale samples at spatial resolutions of a few micrometers to tens of micrometers in a nondestructive manner. The technology has grown in importance in many fields and sectors; for example, it is now routinely used in materials science and areas of manufacturing [1], and it has also emerged as a tool for 3D digital histology [2].

Over the past few years, there has been increasing global interest in implementing micro-CT with amplitude-modulated beams [3–9], which provides two advantages. First and foremost, it enables x-ray phase-contrast imaging (XPCI), a technique that derives contrast from local deformations of the x-ray wave front caused by elastic interactions in the sample (refraction and small-angle scattering) [10]. In conventional micro-CT, contrast is derived from x-ray attenuation, which leads to exquisite images for strongly attenuating materials, but tends to produce a low contrast-to-noise ratio for materials with weak or similar intrinsic attenuation. For many of those materials, refraction-based contrast, as provided by XPCI, can produce a superior contrast-to-noise ratio [11]. Moreover, scattering signals can indicate sample inhomogeneities below the imaging system's spatial resolution [12], thus providing information inaccessible through conventional micro-CT.

Edge illumination (EI) [13,14] and beam tracking (BT) [15–18] are examples of XPCI techniques leveraging amplitude-modulated beams. In these techniques, the sample is irradiated by an array of spatially separated x-ray "beamlets" created by an x-ray-opaque modulator featuring periodic transmitting apertures (Fig. 1). Refraction and scattering cause a shift and broadening of the beamlets, respectively, which are detectable through either a detector with pixels smaller than the beamlets (BT) or a detector with pixels larger than the beamlets (EI) when used in conjunction with a second modulator that functions as an analyzer for the beamlets' directionality and width. BT offers access to separate attenuation,

*Contact author: charlotte.hagen.10@ucl.ac.uk

refraction, and scatter signals from a single sample exposure (a single "shot"), while in EI these signals appear encoded as a convolution with the second modulator. To retrieve them individually, at least three exposures with different offsets between the two modulators are needed [19]. However, if a sample is (quasi)homogeneous (e.g., composed of only one material or several similar materials) and if scatter can be assumed to be absent, a single exposure is sufficient to retrieve a "merged" signal that attenuation and refraction both contribute to; this approach is known as single-shot EI [20].

The second advantage of the use of amplitude-modulated beams relates to spatial resolution. If the beamlets created by the modulator's apertures are narrower, at the plane of the sample, than the effective combined blur produced by the x-ray source and detector [given by the convolution of their respective point-spread functions (PSFs)], and are well separated from each other, then higher spatial frequencies will be transferred compared to the unmodulated case. In other words, the modulator's presence can increase the achievable spatial resolution, a feature called "aperture-driven resolution" [21–23]. Aperture-driven resolution implies that a scanner's resolution limit (normally determined by the source/detector PSF) can be overcome by the use of sufficiently narrow apertures, enabling high-resolution scans with sources and detectors that would otherwise not allow this. Furthermore, since increasing resolution is no longer achieved through magnification, it allows the scanning of larger samples at high resolution than with conventional approaches.

Alongside these advantages, there is also a downside. Since the modulator creates peaks and troughs in the irradiation pattern (with the troughs ideally at, or close to, zero), a single exposure (frame) produces undersampled signals. The undersampling can be severe when a source with an extended focal spot and/or a detector with a broad PSF is used, as a large modulator period is then required to keep the beamlets separated despite the blurring effects. However, undersampling will also occur in the absence of blurring, simply due to the discrete spacing of the beamlets. Consequently, fully sampled datasets cannot be acquired without some form of sample stepping. Typically, the sample is moved in small increments along the lateral direction (the x axis in Fig. 1), a frame is acquired at each step, and a combined projection is built up by the interleaving of the individual frames. Importantly, the step size can be chosen to satisfy the Nyquist-Shannon sampling theorem [24], which states that signals must be sampled at twice their bandwidth to obtain aliasing-free images. However, in a tomographic scan, stepping must be applied at each rotation angle, which enforces a step-and-shoot acquisition and thus makes it incompatible with continuous ("fly") scanning. In a step-and-shoot acquisition, the total scan time is given by the exposure time plus overheads (i.e., the time needed to stop/start the motors and displace and rotate the sample). By contrast, fly scans incur negligible overheads, and the scan time is given by the exposure

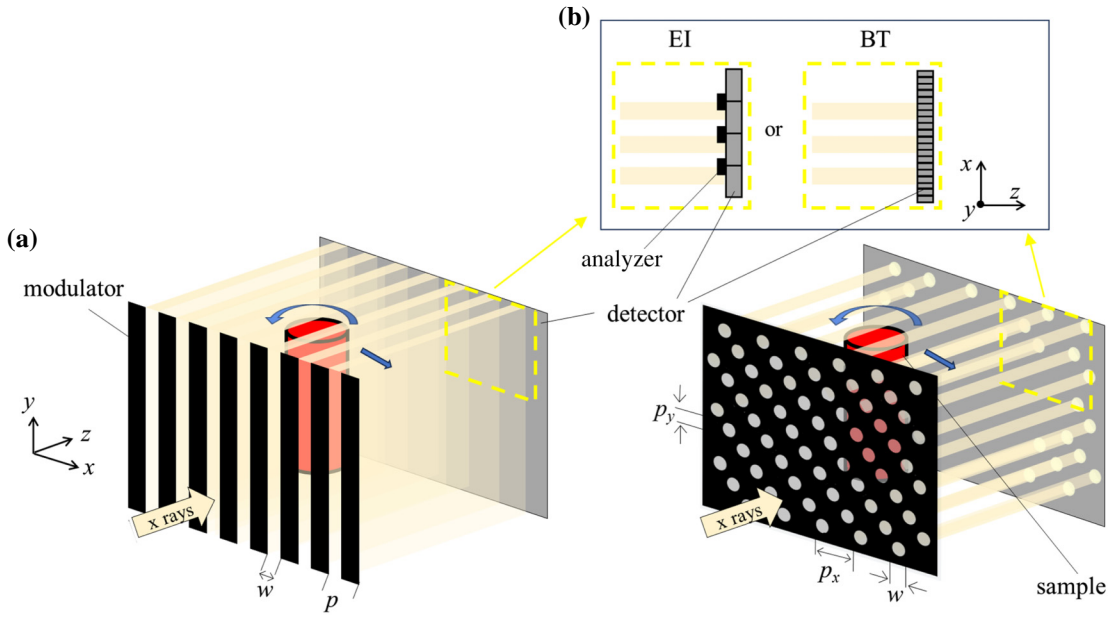

FIG. 1. Micro-CT setups using amplitude-modulated x-ray beams. The two-most-commonly-used modulator designs are shown: (a) slit-shaped apertures and (b) circular apertures arranged in a slanted fashion. Attenuation, refraction, and scattering by the sample causes an amplitude reduction, shift, and broadening of the created beamlets, which can be detected through an EI or a BT approach.

time alone, which makes them much more time-efficient and therefore desirable. Although it is possible to implement stepping through partial fly scans, e.g., by performing a series of continuous rotations each with the sample at a different lateral step, such an acquisition requires that the system and the sample are stable over extended periods, otherwise frames acquired at the different lateral steps, which are now acquired at vastly different times, would be incompatible when combined to form the upsampled projections. For this reason, partial fly scans are not well suited to dynamic scanning, where the sample typically deforms significantly. To enable dynamic micro-CT scanning with amplitude-modulated beams, a fully-fly-scan-compatible solution is required.

Cycloidal computed tomography [25] offers such a solution. A cycloidal scan is characterized by the *simultaneous* translation and rotation of the sample ("roto-translation"), which can be performed continuously, thus allowing one to reduce scan times by eliminating overheads, not dissimilar to the introduction of helical/spiral scanning in clinical CT [26]. Cycloidal scanning shares similarities with the rotation-as-fast-axis (RAFA) technique developed for scanning-probe x-ray microscopy [27,28]. In the RAFA technique, the sample is slowly translated through a focused or collimated beam without interruption while it is continuously and repeatedly rotated through 360°. In cycloidal scanning, a single full rotation of the sample is sufficient, but the sample is repeatedly translated across the modulator period, to bridge the gaps between adjacent beamlets (see Ref. [29] for illustrations of cycloidal trajectories). The previously cited articles have shown that cycloidal scanning preserves compatibility with XPCI and some degree of aperture-driven resolution, but results were qualitative. This article presents a quantitative analysis of cycloidal scanning by presenting a theoretical framework and deriving sampling conditions that are optimal in the sense of the Nyquist-Shannon theorem. These conditions are experimentally implemented and quantitatively analyzed on the basis of their modulation transfer. It is shown that Nyquist-compliant cycloidal sampling achieves full aperture-driven resolution, close to the theoretical limit given by the modulator's aperture width, and provides the same image quality as stepping, but in a more-time-efficient manner. The theoretical framework and the derived sampling conditions are widely applicable (e.g., to beam tracking, edge illumination, and implementations with laboratory and synchrotron sources) and can be adapted to the RAFA technique.

II. PREREQUISITES

A. System geometry and assumptions

Consider a micro-CT setup as shown in Fig. 1(a) or Fig. 1(b), featuring an x-ray-opaque modulator with transmitting apertures of width w, spaced periodically with period p. The beam modulation can be one dimensional, based on slit-shaped apertures, or two dimensional, based on (most commonly) circular apertures. In a tomographic setting, the lateral beam modulation (i.e., along the x axis) defines the achievable resolution within the reconstructed axial slices (in-slice resolution), while a beam modulation along the y axis can redefine the slice thickness and out-of-slice resolution. Cycloidal scanning, by which the sample is translated along the x axis while it is rotated around the y axis, alleviates the lateral undersampling, but does not impact on sampling along the y axis (the latter would require a "cycloidal-spiral" approach [30]). Since the focus here is on cycloidal scanning, it is assumed that signals are undersampled laterally but well-sampled along the y axis. This is usually achieved with slit-shaped apertures, as the frequency transfer along the y axis is determined by the source/detector PSF for which the pixel pitch provides an adequate sampling rate. But it is also achieved with circular apertures when these are arranged in a slanted manner [31]; the frequency transfer is now defined by the aperture in both directions; however, a smaller separation between beamlets along the y axis at the expense of an increased separation along the x axis ensures a sufficiently fine out-of-slice sampling.

The following further assumptions ensure that the conditions for aperture-driven resolution are met. First, the modulator's aperture width w is smaller than the full width at half maximum (FWHM) of the x-ray source's focal spot when it is projected to the detector and then scaled to the modulator. Second, the modulator's period p is sufficiently large to ensure that there is no, or minimal, overlap between adjacent beamlets. Third, minimal signal diffusion occurs during detection; that is, the crosstalk between neighboring pixels is sufficiently small. Since our aim is to enable fly scans, a (key) fourth assumption is that XPCI signals are retrievable from a single frame, which is possible through BT or single-shot EI. Finally, we restrict the imaging geometry to a parallel-beam scenario or small cone angle; in the latter case, we consider the modulator and sample to lie in the same plane, which allows omission of the magnification factor between the two planes from the equations.

Although other XPCI techniques exist (e.g., grating interferometry [32] and speckle tracking [33]), the requirements for aperture-driven resolution and cycloidal sampling are not necessarily met for those techniques, as they do not use distinct, physically separated beamlets. Thus, resolution in those techniques remains a function of the detector point-spread function, and the sampling rate given by the pixel pitch is typically adequate.

B. Theoretical framework

Since adequate out-of-slice sampling is assumed, we seek to derive optimal sampling conditions for

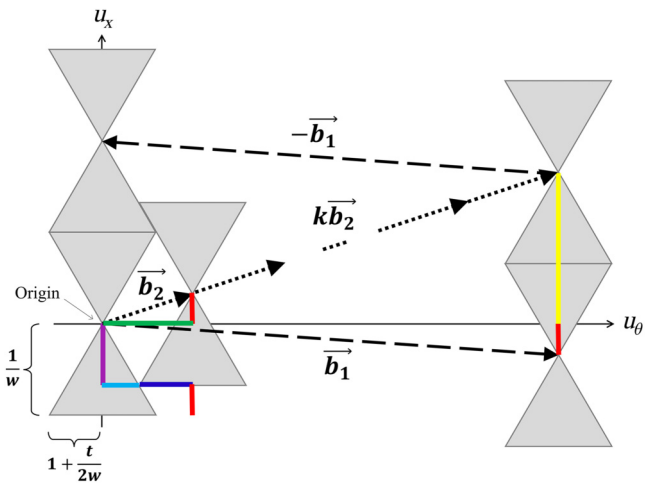

FIG. 2. Arrangement of shifted replica of the bow-tie-shaped sinogram support in Fourier space.

two-dimensional sinograms, which are functions of the lateral and angular coordinate: $S(x,\theta)$. To understand how to best sample a function of this type, we need to know its support in the Fourier domain, i.e., the size and shape of the area around the Fourier domain's origin beyond which any frequency content can be considered negligible. A sinogram's Fourier domain support is bow tie shaped [34]. Previous work [35] confirmed that this applies also to amplitude-modulated beams, and that in this case, within the approximation that an aperture of width w transfers frequencies of up to $1/w$, the support (shown in Fig. 2) is given by the set of frequencies (u_x, u_θ) adhering to

$$|u_x| < \frac{1}{w}, \tag{1}$$

$$|u_\theta| < 1 + \frac{|u_x| t}{2}, \tag{2}$$

where t is the sample thickness in the x-z plane.

A tomographic scan can be thought of as sampling the function $S(x,\theta)$ in discrete points on the lateral and angular axes. Mathematically, this sampling process can be described as a multiplication of S with a Dirac comb (in the following referred to as a "grid") spanned by two vectors:

$$\vec{a_1} = \begin{bmatrix} \Delta\theta \\ d \end{bmatrix}, \quad \vec{a_2} = \begin{bmatrix} \Delta\theta \\ \Delta x - d \end{bmatrix}, \tag{3}$$

where $\Delta\theta$ is the angular sampling step, Δx is the lateral sampling step, and d introduces an offset to the lateral sampling points that is applied for each value of $\Delta\theta$. The parameter d includes tilted sampling grids, while rectangular sampling grids are naturally included as they correspond to $d = 0$. Now the question arises as to how $\Delta\theta$, Δx, and d should be chosen to accurately capture the frequency content of S.

In the Fourier domain, sampling can be described as a convolution of the sinogram's frequency spectrum with a reciprocal sampling grid, spanned by the vectors

$$\vec{b_1} = \begin{bmatrix} \frac{1}{\Delta\theta}\left(1 - \frac{d}{\Delta x}\right) \\ -\frac{1}{\Delta x} \end{bmatrix}, \quad \vec{b_2} = \begin{bmatrix} \frac{1}{\Delta\theta}\frac{d}{\Delta x} \\ \frac{1}{\Delta x} \end{bmatrix}. \tag{4}$$

The convolution creates shifted replicas of the data confined to the bow-tie-shaped support, located in the reciprocal grid points. The shifted replicas may be thought of as "tiles", and in this sense, sampling can be understood as "tiling" the Fourier domain with bow ties. Since aliasing is defined as overlap occurring between the shifted replicas, the tiling framework provides an immediate condition for optimal sampling, i.e., select those values of $\Delta\theta$, Δx, and d that lead to the densest tiling without overlap.

III. RESULTS

A. Optimal sampling conditions for cycloidal scanning

On the basis of the framework described above, it can easily be derived that rectangular sampling ($d = 0$) can achieve a no-overlap scenario if the sample is rotated in angular increments of $\Delta\theta = (2 + t/w)^{-1}$ and, at each angle, moved along the lateral direction in steps of half the aperture width, i.e., $\Delta x = w/2$ [35]. Further, it is known that the densest Fourier space tiling is achieved for so-called interlaced sampling [34], as this optimally exploits the tiles' bow-tie shape. Optimal interlaced sampling involves rotating the sample in angular increments of $\Delta\theta = (4 + t/w)^{-1}$ and, at each angle, moving it laterally in steps of $\Delta x = w$, but also applying an offset of $d = w/2$ between the lateral sampling steps for each angle [35].

As explained above, when amplitude-modulated beams are used, rectangular and interlaced sampling can be realized only through (at least partial) step-and-shoot scans, as the sample has to be kept in a fixed rotational position during the lateral translation, or in a fixed lateral position during the rotation. For a sampling scheme to be fully-fly-scan compatible, it must not involve any lateral translation of the sample at a fixed rotational position or vice versa. Instead, the sample translation must be performed *concurrently* with its rotation, which is fulfilled for a cycloidal scan. To describe a cycloidal scan mathematically, we can again make use of the grid vectors in Eqs. (3) and (4). However, in contrast to rectangular or interlaced sampling, in cycloidal sampling the lateral sampling step is fixed to the modulator's period, i.e., $\Delta x = p$. The lateral sample translation, performed concurrently with the rotation by $\Delta\theta$, is now described via the offset parameter d. These latter two parameters ($\Delta\theta$ and d)

TABLE I. Optimal sinogram sampling conditions for micro-CT with amplitude-modulated beams. The conditions are stated for rectangular, interlaced, and cycloidal sampling. The angular step is expressed in radians. The column headed "N_π" states the total number of frames required for optimal sampling when a sample rotation over π is assumed.

	$\Delta\theta$	Δx	d	N_π	Fly-scan compatible?
Rectangular	$\dfrac{1}{(2+\frac{t}{w})}$	$\dfrac{w}{2}$	0	$\pi\left(2+\dfrac{t}{w}\right)\left(\dfrac{2p}{w}\right)$	Partially
Interlaced	$\dfrac{1}{(4+\frac{t}{w})}$	w	$\dfrac{w}{2}$	$\pi\left(4+\dfrac{t}{w}\right)\left(\dfrac{p}{w}\right)$	Partially
Cycloidal	$\dfrac{1}{\left(2+\frac{t}{w}-\frac{t}{2p}\right)\left(\frac{2p}{w}\right)}$	p	$\dfrac{w}{2}$	$\pi\left(2+\dfrac{t}{w}-\dfrac{t}{2p}\right)\left(\dfrac{2p}{w}\right)$	Fully

must still be chosen, and, in analogy to rectangular or interlaced sampling, the optimal choice is the one that leads to the densest arrangement of bow ties without them overlapping. The optimal parameters can be found via geometrical considerations, as illustrated in Fig. 2. Consider two bow ties immediately adjacent to the central one, e.g., those located at grid points $\vec{b}_2$ and $-\vec{b}_1+k\vec{b}_2$, where $k=((1/\Delta\theta)(1-d/p)/(1/\Delta\theta)(d/p))=((p/d)-1)$. The bow tie at the latter grid point is aligned with the central one along u_θ but shifted along u_x. To avoid overlap with the central bow tie, the u_x shift, which is given by the lengths of the red and yellow segments combined, must be equal to or greater than the bow-tie height of $2/w$. The lengths of the red and yellow segments are $1/p$ and k/p, respectively, which sums to $k+1/p=1/d$. We therefore find

$$\frac{1}{d}\geq\frac{2}{w}\quad\Leftrightarrow\quad d\leq\frac{w}{2}. \tag{5}$$

For the bow tie located at grid point $\vec{b}_2$, it can be seen that its shift along u_x (red segment) relative to the central bow tie is defined by $1/p$ and is thus fixed. Its shift along u_θ is given by the green segment, which has a length of $(1/\Delta\theta)(d/p)$. To avoid overlap with the central bow tie, the green segment must be at least as long as the light-blue and dark-blue segments combined, where the dark-blue segment has a length of $1+(t/2w)$. The length of the light-blue segment can be calculated from Eq. 2, by realizing that $w_x=(1/w)-(1/p)$ (purple segment) at this position, for which $u_\theta=1+((1/w-1/p)\,t/2)$. We therefore find

$$\frac{1}{\Delta\theta}\frac{d}{p}\geq 1+\frac{t}{2w}+1+\frac{t}{2}\left(\frac{1}{w}-\frac{1}{p}\right)=2+\frac{t}{w}-\frac{t}{2p}, \tag{6}$$

and assuming $d=w/2$ (to achieve the densest possible tiling along u_x),

$$\begin{aligned}&\frac{1}{\Delta\theta}\geq\left(2+\frac{t}{w}-\frac{t}{2p}\right)\left(\frac{2p}{w}\right)\\ \Leftrightarrow\quad&\Delta\theta\leq\frac{1}{\left(2+\frac{t}{w}-\frac{t}{2p}\right)\left(\frac{2p}{w}\right)}.\end{aligned} \tag{7}$$

The expressions for the optimal $\Delta\theta$ and d are the key theoretical result of this article; they are summarized in Table I (bottom row) alongside the optimal conditions for rectangular (top row) and interlaced sampling (middle row). The real-space grids and Fourier-domain tilings corresponding to the optimal conditions for the three schemes are illustrated in Fig. 3. It can be seen that optimal interlaced sampling corresponds to the densest coverage of the Fourier domain, or, in other words, it can be realized with the fewest number of frames. Optimal rectangular

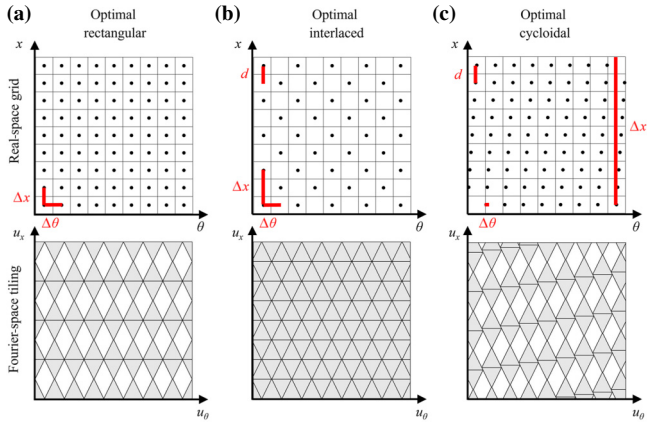

FIG. 3. Optimal sinogram sampling in real space (top row) and the Fourier domain (bottom row) for micro-CT with amplitude-modulated beams for (a) rectangular, (b) interlaced, and (c) cycloidal sampling. The illustration was created by our assuming that $p/w=8$ and $t=1$ mm.

sampling requires approximately twice as many frames as interlaced sampling. In cycloidal sampling, the tiling density depends on the ratio between p (the modulator's period) and w (the modulator's aperture width). Generally, a cycloidal tiling is less dense than an interlaced one, but denser than a rectangular one, thus requiring fewer frames than the latter. The optimality of the derived conditions was confirmed through a simulation study, which is presented in Supplemental Material [36].

B. Experimental implementation of optimal cycloidal fly scans: Modulation-transfer analysis

A custom-built micro-CT system was used to implement the derived sampling conditions. The system components and parameters are summarized in Table II. Although this system implements single-shot EI and operates with a laboratory source, the optimal conditions are general and also apply to systems implementing BT.

A first set of experiments investigated the transition from optimal cycloidal step-and-shoot scans to fly scans. The former can be implemented by one translating the sample laterally by distance d and rotating it by angle $\Delta\theta$ with the sample being left stationary while the frames are acquired. Owing to the modulators' and pixel array's periodicity, the translation may be unidirectional, i.e., the sample can be moved "forward" in steps of d until the scan is complete. However, this requires a relatively large field of view, as the sample must remain fully contained in it at all times. To avoid this requirement, the sample is usually translated in steps of d by one modulator period (i.e., bridging the gaps between adjacent beamlets), placed back in its initial position ("reset"), again translated in steps of d by one modulator period, and so on. We call this sequence "cycloidal forward only" due to its equivalence to a true forward-only scheme. While convenient for a step-and-shoot scan, the resets imply that this acquisition sequence cannot be realized as a full fly scan. However, the sequence can be approximated in a fully-fly-scan-compatible manner by one translating the sample in steps of d by one modulator period, then translating it "backwards" in steps of $-d$ by one modulator period, again translating it in steps of d by one modulator period, and so on [29]. We call this sequence "cycloidal back and forth." The back-and-forth scheme is not limited to translating the sample within a single modulator period, and the translation can also span multiple periods. This has the advantage that systematic errors caused by, for example, local variations in the detector or the modulator's apertures, which would lead to ring artifacts, are "smeared out" during image reconstruction. At the same time, the number of modulator periods traversed should be sufficiently small for the sample to remain within the field of view. A back-and-forth translation within ten modulator periods was found to be a reasonable compromise, and this was applied in all cycloidal back-and-forth scans reported in this article. Cycloidal back-and-forth scans were implemented first as step-and-shoot scans and then as fly scans.

To quantitatively compare the three acquisition schemes (cycloidal forward-only step-and-shoot scan, cycloidal back-and-forth step-and-shoot scan, and cycloidal back-and-forth fly scan), we applied them to scans of a commercial resolution phantom [micro-CT bar-pattern (air) phantom, QRM, Germany]. The phantom consists of a square silicon chip of size 5×5 mm^2 located inside a plastic cylinder of 20-mm diameter, aligned with one of its axial planes (the phantom contains a second chip oriented vertically, but this was not used). The chip features a series of test structures (bar and point patterns) with sizes ranging from 5 to 150 μm. The optimal cycloidal-sampling conditions for this phantom were calculated from its

TABLE II. Components and parameters of the custom-built micro-CT system.

X-ray source	MicroMax-007 HF (Rigaku, Japan); rotating Mo anode (40 kVp, 20 mA)
Focal spot	70 μm (FWHM; lateral dimension)
Energy	Polychromatic; mean energy approximately 18 keV
Detector	C9732DK CMOS-based flat panel (Hamamatsu, Japan); 2368 × 2340 pixels
Pixel size	50×50 μm^2
Detector PSF	120 μm (FWHM; estimated for an identical detector [37])
Modulator	Gold (160 ± 40 μm thick) electroplated onto a graphite substrate (1-mm thick) (Microworks, Germany) Slit-shaped apertures of 12-μm width, 76-μm period Placed with 12-μm lateral offset to the analyzer
Analyzer[a]	Gold (150 ± 40 μm thick) electroplated onto graphite substrate (1 mm thick) (Microworks, Germany) Slit-shaped apertures of 20 μm width, 96 μm period Apertures aligned with the pixel centres
Source-detector distance	0.865 m
Source-sample distance	0.708 m
Source-modulator distance	0.633 m
Source-analyzer distance	0.828 m

[a]Enables EI (Fig. 1); is a scaled replica of the modulator.

TABLE III. Optimal sampling conditions for the scanned samples.

	$\Delta\theta$ (mrad)	Δx (μm)	d (μm)	$N_{2\pi}$
		Resolution phantom		
Rectangular	1.603671594	6.24	0	50 934
Cycloidal	0.1338841958	81.2	6.24	46 930
		Cocktail stick		
Rectangular	6.327477651	6.24	0	12 909
Cycloidal	0.5282207068	81.2	6.24	11 895
		Esophageal scaffold		
Rectangular	1.774911104	6.24	0	46 020
Cycloidal	0.1481673656	81.2	6.24	42 406

thickness t, the first modulator's period p, and the modulator's aperture width w. As thickness, we would normally consider the full sample diameter; however, in this case all relevant information was contained in the chip, and therefore we considered the diagonal dimension of the chip. Since the phantom's center was positioned 0.45 mm from the axis of rotation (due to the difficulty in positioning it exactly at the axis of rotation), twice this distance was added to the chip dimension, yielding a total effective sample thickness t of $(\sqrt{2} \times 5 + 2 \times 0.45)$ mm $= 7.971$ mm. The modulator parameters p and w had to be scaled to the sample plane before they entered the calculation. The resulting optimal conditions are summarized in Table III. To provide a benchmark for the three cycloidal scans, we also implemented optimal rectangular step-and-shoot sampling.

The exposure time per frame was 2 s for all scans. Dark-field images were acquired before each scan. For the cycloidal and rectangular step-and-shoot scans, flat-field images were acquired at an interval of 13 000 acquired frames. For the cycloidal fly scans, flat-field images were acquired before and after the scan. A knife-edge method was used to track the lateral position of the sample during the fly scan; this ensures accurate knowledge of the sample's trajectory even when this deviates from the nominal trajectory, such as when the translation motor decelerates and accelerates at the "turnaround" points of the cycloidal back-and-forth scans. This method is described elsewhere [38], but briefly, it consists in one affixing a scraper blade to the sample's translation stage (but not on the rotation stage) at an angle to the x axis and using the subpixel position extracted from the blade's profile to locate the sample. In the cycloidal forward-only and rectangular scans, a "jittering" sequence was implemented, by which the sample is displaced by a pseudorandom integer multiple of d or Δx at each angle, to "smear out" the effect of systematic errors to avoid ring artifacts, thus producing an effect similar to that achieved by extension of a cycloidal back-and-forth scan over multiple modulator periods. Image processing involved dark-field and flat-field corrections, geometrical correction of the sinograms (required when the sample translation exceeds one modulator period, see Ref. [38]), bivariate cubic interpolation (cycloidal sinograms only, to rearrange the data on a rectangular grid), and single-shot-EI retrieval [20]. After interpolation, rectangular and cycloidal sinograms have the same size. Tomographic reconstruction was performed with the Feldkamp-David-Kress algorithm [39], motivated by the fact that the experimental system features a small cone angle.

Figure 4 shows the tomographic images obtained via the different acquisition sequences (first row). Note that the cycloidal-scan images were reconstructed from fewer frames than the rectangular-scan ones and thus may appear slightly noisier, as the exposure per frame was the same in all cases. We performed a quantitative modulation-transfer-function (MTF) analysis on these images, following application of a beam-hardening correction algorithm [40] to improve the modulation estimates. Modulation was assessed from the central set of vertical bar patterns (second row). Average profiles across these central-set patterns were calculated (third row). There are six patterns featuring bar sizes of 30, 25, 20, 15, 10, and 5 μm, and representing spatial frequencies of 16.67, 20, 25, 33.33, 50, and 100 lp/mm. Each pattern consists of five line pairs. Although, strictly speaking, the MTF is defined as the modulation of sinusoidal patterns, here it is measured with square-wave patterns, since the bars in the phantom have a rectangular shape. Such a substitution is known to cause a slight overestimation of modulation at certain spatial frequencies, due to the presence of higher-harmonic terms. This effect explains the observed increased "peaks" and decreased "valleys" in the profiles across the 15-μm and 20-μm bar patterns. To estimate the modulation, the maximum and minimum image gray values were extracted for five pairs of "peaks" and "valleys" in a pattern. This procedure was applied for 20 horizontal profiles across the patterns, such that 100 modulation values were available per spatial frequency. The values were normalized by the modulation extracted at a relatively low spatial frequency, where it is expected to approach unity (here, 16.67 lp/mm). Finally, the mean of the 100 available values was calculated, and is plotted (fifth row in Fig. 4) with error bars that represent 1 standard deviation. The MTF analysis was complemented by the edge method, whereby an edge profile is extracted from each of the reconstructed images (here, across the vertical blue line in the top-left panel), an error function is fitted, and its derivative is computed, resulting in the line-spread function from which the MTF was found by taking the Fourier transform. The edge method has the advantage that MTF values are available for a much-finer-sampled-spatial-frequency axis. The extracted edge profiles are shown (fourth row in Fig. 4).

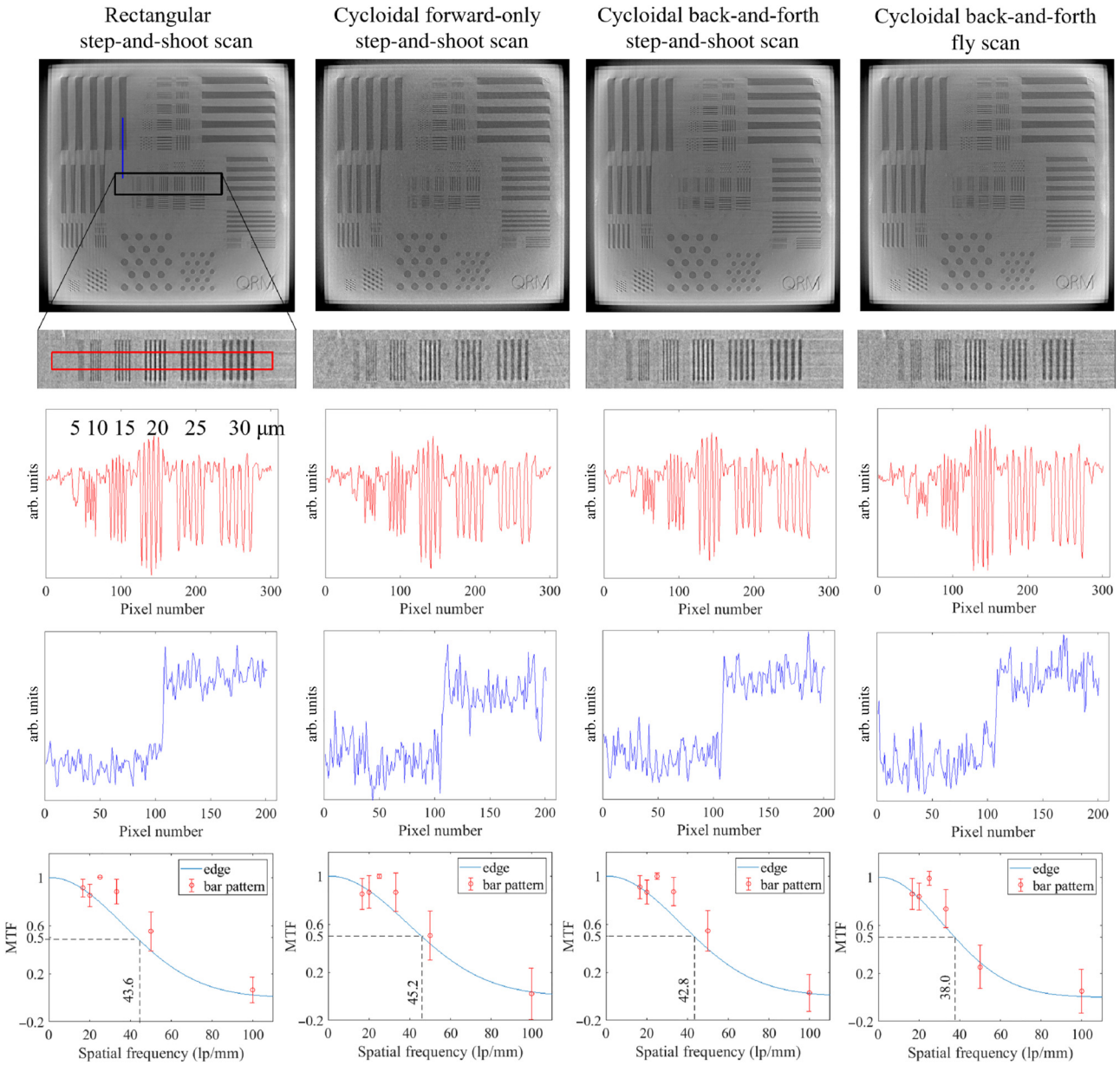

FIG. 4. First row: Tomographic images of the resolution phantom (scale bar not shown, but images show a scale of approximately 5×5 mm^2). Second row: Enlarged regions showing only the central bar patterns. Third row: Profile plots obtained by our averaging vertically over the central bar patterns. Fourth row: Edge profiles (extracted from the region indicated by the blue line in the top-left panel). Fifth row: MTF as extracted from the edge (blue line) and from the bar pattern (red circles along with error bars).

The resulting MTF curves are plotted alongside the results from the bar-pattern analysis (fifth row in Fig. 4).

The results obtained with the two methods largely agree, within uncertainties. Exceptions are the MTF values calculated from the 25- and 33.33-lp/mm bar patterns, which are notably higher than the values calculated from the edge; we believe this discrepancy stems from the above-mentioned use of square-wave patterns. The 50% MTF threshold, often considered a conservative estimate of spatial resolution, occurs at a similar spatial frequency for all step-and-shoot scans (43.6, 45.2, and 42.8 lp/mm), confirming that cycloidal and rectangular schemes can be considered equivalent in terms of their modulation transfer. It can be seen that the 50% MTF threshold for the cycloidal fly scan occurs at a slightly lower spatial frequency, at 38.0 lp/mm, which we believe is representative of the motion blur that is usually observed when a continuously moving sample is imaged. Since the corresponding real-space resolution (13.2 µm) is near the theoretical limit of aperture-driven resolution, given by the aperture width

scaled to the sample plane (12.814 μm), the optimal performance appears to be preserved aside from the motion blur.

C. Application to samples with intricate natural structure

Subsequent experiments focused on our applying the results on two samples that display intricate natural structure; a wooden cocktail stick of 2-mm diameter, and a piglet esophagus scaffold derived via decellularization (see Ref. [41] for details on this sample and its preparation) contained in a 6-mm plastic cylinder. For these samples, rectangular step-and-shoot scans and cycloidal back-and-forth fly scans were performed. Optimal cycloidal and rectangular sampling conditions were calculated (Table III) on the basis of the samples' diameters and their (slight) offset from the axis of rotation. The exposure time per frame was again 2 s for all scans, and scans were performed and images processed as described above. The reconstructed images are shown in Fig. 5. It can be seen that, apart from a slight motion blur, the images resulting from cycloidal fly scans are of comparable quality to those resulting from the rectangular step-and-shoot scans, with intricate details resolved almost equally well in both.

D. Scan-time reductions

At this point, we reiterate that the advantage of fly scans over step-and-shoot scans is their greater scan-time efficiency. The relative gain in scan time achieved when rectangular step-and-shoot scans are replaced by cycloidal fly scans depends on the way the former are performed. If the detector is read out for every frame, then overheads (i.e., readout times) are independent of exposure times, and so the shorter the exposure time, the greater the relative gain. This will be most significant at synchrotrons, where exposure times tend to be very short. In our case, however, we did not read out the detector for every frame, but kept all frames in memory until after the scan. To implement a stepped translation and rotation of the sample, we doubled the number of frames and used every other frame as a "spacer" during which the sample was repositioned; the sample would then be in a stationary position for the following frame. Only the frames for which the sample was in a stationary position were used for forming the image. The relative scan-time gain enabled by a cycloidal fly scan is now slightly greater than a factor of 2, as cycloidal sampling requires slightly fewer frames than rectangular sampling and the "spacer frames" are no longer needed. All fly scans reported above were thus approximately 2 times faster than their step-and-shoot counterparts. Note that the "spacer-frame" strategy can be applied only if the spacer frames are of sufficiently long duration to reposition the sample, making it a less-suitable option when one working with very short exposure times.

The scans reported so far were performed with relatively long total exposures [e.g., 23.5 h for the esophageal scaffold shown in Fig. 5(d)], which are in part a result of our using a laboratory x-ray source, which offers significantly less flux than, for example, a synchtrotron, and in part because we wanted to ensure that the analyses and observations on sampling and resolution were minimally

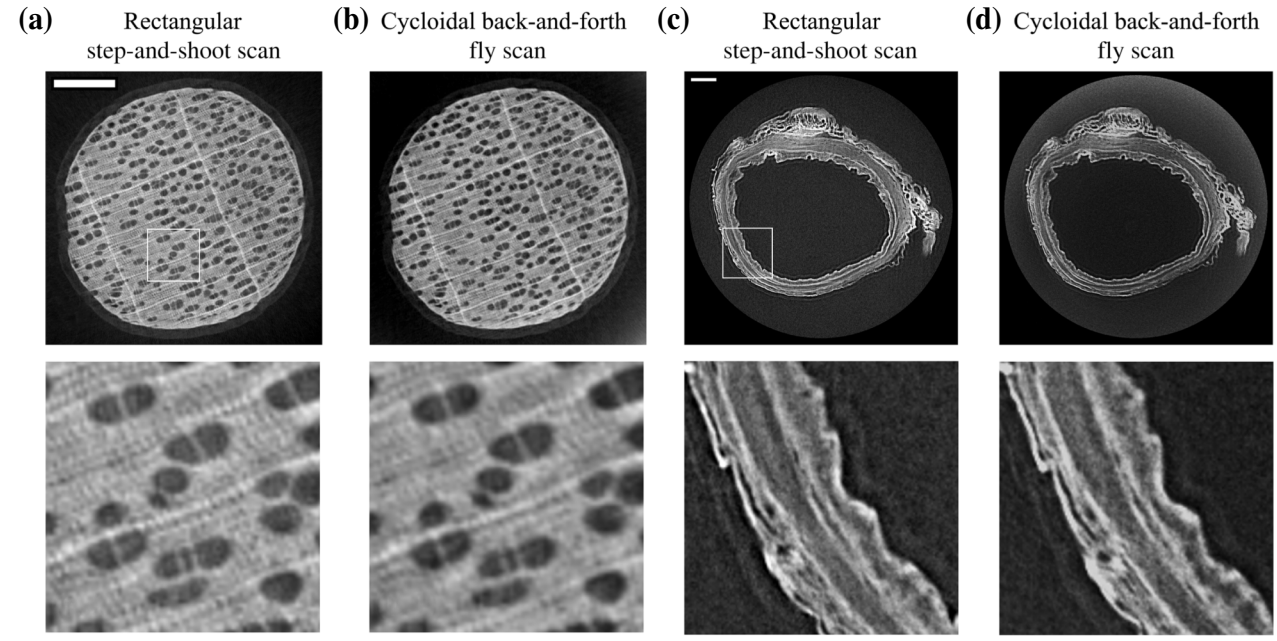

FIG. 5. Tomographic images reconstructed from rectangular step-and-shoot scans and cycloidal back-and-forth fly scans showing (a),(b) the cocktail stick and (c),(d) the esophageal scaffold . Both scale bars indicate 0.5 mm.

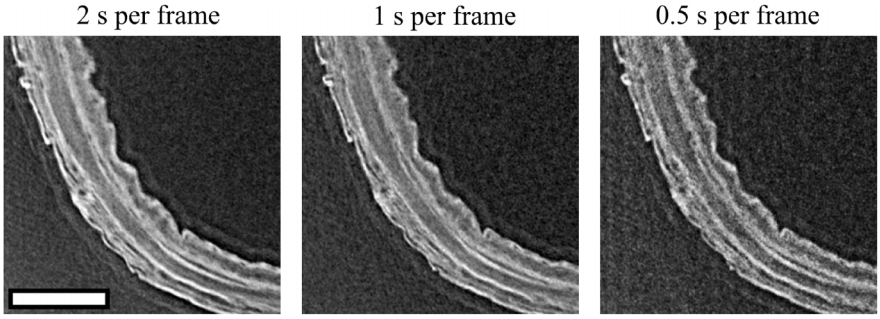

FIG. 6. Tomographic images (close-up) of the esophageal scaffold acquired with optimal cycloidal back-and-forth fly scans with gradually reduced exposure times per frame. The scale bar indicates 0.5 mm.

affected by high levels of noise. We acknowledge that such long exposures may be considered impractical or even unrealistic in some contexts, and we therefore performed additional cycloidal fly scans with reduced exposure times. The esophageal scaffold was rescanned with 1- and 0.5-s exposures per frame, corresponding to total exposures and therefore scan times of 11.8 and 5.9 h, respectively (the corresponding rectangular step-and-shoot scans, which are not shown, would be approximately twice as long). The resulting images are shown in Fig. 6, showing that noise is increased as the exposure time is reduced; however, since the optimal cycloidal sampling conditions were adhered to in all cases, resolution is preserved. As the 0.5-s-per-frame image still shows an acceptable SNR, we believe that greater noise levels may be tolerated and that, therefore, even shorter exposures could be used (in our case, this was prevented by the maximum frame rate of the detector, which is 2.5 frames per second). This implies that for samples similar to the one shown here (i.e., weakly attenuating biological samples of up to 1 cm in diameter) optimally sampled cycloidal fly scans can be completed within a couple of hours with a laboratory source, all while preserving compatibility with XPCI and achieving spatial resolutions in the 10–20-μm range. At synchrotrons, where there is an abundance of flux, scan times for a corresponding imaging task or an even higher spatial resolution, would be significantly shorter.

IV. CONCLUSION

We have presented a quantitative treatment of cycloidal computed tomography, a method that facilitates the implementation of time-efficient fly scans in micro-CT with amplitude-modulated beams. In particular, we have derived sampling conditions that satisfy the Nyquist-Shannon sampling theorem, based on knowledge on the sinogram's support in the Fourier domain and geometrical considerations. It was shown that these conditions enable (in-slice) spatial resolutions close to the theoretical limit determined by the size of the apertures in the modulator, in both step-and-shoot-scan and fly-scan implementations, and that resolution is preserved when the total exposure is reduced. While absolute scan times ultimately depend on the setup (e.g., laboratory or synchrotron), the imaging task (e.g., noise tolerance), the sample (e.g., via its thickness and composition), and the scripting of the acquisition, in relative terms fly scans will always be faster than step-and-shoot scans. The availability of fly-scan-compatible optimal sampling conditions for micro-CT with amplitude-modulated beams is therefore of key importance in areas where scan times have traditionally been long, such as laboratory-based XPCI acquisitions, or to facilitate high-speed scans at synchrotrons to ultimately enable dynamic imaging.

The data that support the findings of this study are available from the contact author upon reasonable request.

ACKNOWLEDGMENTS

This work was supported by EPSRC (Grants No. EP/T005408/1 and No. EP/T029080/1). C.K.H. is supported by the Royal Academy of Engineering under the Research Fellowship scheme. A.O. is supported by the Royal Academy of Engineering under the Chairs in Emerging Technologies scheme (Grant No. CiEI1819/2/78). This work was also supported by the national research facility for laboratory-based x-ray CT (NXCT) through EPSRC Grant No. EP/T02593X/1.

A.C. and D.B. are Nikon employees. M.E., A.O., and C.H. are named inventors on patents owned by University College London protecting the imaging technology used to obtain the results presented.

[1] P. J. Withers, C. Bouman, S. Carmignato, V. Cnudde, D. Grimaldi, C. K. Hagen, E. Maire, M. Manley, A. Du Plessis, and S. R. Stock, X-ray computed tomography, Nat. Rev. Methods Primers **1**, 18 (2021).

[2] O. L. Katsamenis, M. Olding, J. A. Warner, D. S. Chatelet, M. G. Jones, G. Sgalla, B. Smit, O. J. Larkin, I. Haig,

L. Richeldi, I. Sinclair, P. M. Lackie, and P. Schneider, X-ray micro-computed tomography for nondestructive three-dimensional (3D) X-ray histology, Am. J. Pathol. **189**, 1608 (2019).

[3] C. Zhang, C. Li, J. Qi, H. Shang, X. Pan, and G. Li, Simulations of single-shot X-ray phase-contrast tomography based on edge illumination, Nucl. Instrum. Methods Phys. Res. A: Accel. Spectrom. Detect. Assoc. Equip. **983**, 164598 (2020).

[4] A. Pil-Ali, S. Adnani, C. Scott, and K. Karim, in *Proc. SPIE 11595*, Medical Imaging 2021: Physics of Medical Imaging 115951N (SPIE, 2021).

[5] J. Yuan, I. Harmon, and M. Das, in *Proc. SPIE PC12031*, Medical Imaging 2022: Physics of Medical Imaging PC120310X (SPIE, 2022).

[6] A. Hurlock, T. Koh, M. Martinez, and M. Gehm, in *Proc. SPIE 12531*, Anomaly Detection and Imaging with X-Rays (ADIX) VIII 125310F (SPIE, 2023).

[7] L. Brombal, F. Arfelli, R. H. Menk, L. Rigon, and F. Brun, PEPI Lab: A flexible compact multi-modal setup for X-ray phase-contrast and spectral imaging, Sci. Rep. **13**, 4206 (2023).

[8] P. Vanthienen, J. Sanctorum, B. Huyge, N. Six, J. Sijbers, and J. De Beenhouwer, Grating designs for cone beam edge illumination X-ray phase contrast imaging: A simulation study, Opt. Express **31**, 28051 (2023).

[9] N. Six, J. Renders, J. De Beenhouwer, and J. Sijbers, Joint multi-contrast CT for edge illumination X-ray phase contrast imaging using split Barzilai-Borwein steps, Opt. Express **32**, 1135 (2024).

[10] S. W. Wilkins, Y. I. Nesterets, T. E. Gureyev, S. C. Mayo, A. Pogany, and A. W. Stevenson, On the evolution and relative merits of hard X-ray phase-contrast imaging methods, Philos. Trans. R. Soc. A **372**, 20130021 (2014).

[11] M. Kitchen, G. Buckley, T. Gureyev, M. Wallace, N. Andres-Thio, K. Uesugi, N. Yagi, and S. Hooper, CT dose reduction factors in the thousands using X-ray phase contrast, Sci. Rep. **7**, 15953 (2017).

[12] P. Modregger, M. Kagias, S. Irvine, R. Broennimann, K. Jefimovs, M. Endrizzi, and A. Olivo, Interpretation and utility of the moments of small-angle x-ray scattering distributions, Phys. Rev. Lett. **118**, 265501 (2017).

[13] A. Olivo, Edge-illumination x-ray phase-contrast imaging, J. Phys. Condens. Matter **33**, 363002 (2021).

[14] C. K. Hagen, P. R. T. Munro, M. Endrizzi, P. C. Diemoz, and A. Olivo, Low-dose phase contrast tomography with conventional x-ray sources, Med. Phys. Lett. **41**, 070701 (2014).

[15] F. A. Vittoria, M. Endrizzi, P. C. Diemoz, A. Zamir, U. H. Wagner, C. Rau, I. K. Robinson, and A. Olivo, X-ray absorption, phase and dark-field tomography through a beam tracking approach, Sci. Rep. **5**, 16318 (2015).

[16] F. A. Vittoria, G. K. N. Kallon, D. Basta, P. C. Diemoz, I. K. Robinson, A. Olivo, and M. Endrizzi, Beam tracking approach for single-shot retrieval of absorption, refraction, and dark-field signals with laboratory x-ray sources, Appl. Phys. Lett. **106**, 224102 (2015).

[17] C. Navarrete-León, A. Doherty, S. Savvidis, M. F. M. Gerli, G. Piredda, A. Astolfo, D. Bate, S. Cipiccia, C. K. Hagen, A. Olivo, and M. Endrizzi, X-ray phase-contrast microtomography of soft tissues using a compact laboratory system with two-directional sensitivity, Optica **10**, 880 (2023).

[18] F. A. Vittoria, M. Endrizzi, P. C. Diemoz, U. H. Wagner, C. Rau, I. K. Robinson, and A. Olivo, Virtual edge illumination and one dimensional beam tracking for absorption, refraction, and scattering retrieval, Appl. Phys. Lett. **104**, 134102 (2014).

[19] M. Endrizzi and A. Olivo, Absorption, refraction and scattering retrieval with an edge-illumination-based imaging setup, J. Phys. D: Appl. Phys. **47**, 505102 (2014).

[20] P. C. Diemoz, C. K. Hagen, M. Endrizzi, M. Minuti, R. Bellazzini, L. Urbani, P. De Coppi, and A. Olivo, Single-shot x-ray phase-contrast computed tomography with nonmicrofocal laboratory sources, Phys. Rev. Appl. **7**, 044029 (2017).

[21] P. C. Diemoz, F. A. Vittoria, and A. Olivo, Spatial resolution of edge illumination X-ray phase-contrast imaging, Opt. Express **22**, 15514 (2014).

[22] A. Zekavat, G. Lioliou, O. Roche i Morgo, C. Maughan Jones, G. Galea, E. Maniou, A. Doherty, M. Endrizzi, A. Astolfo, A. Olivo, and C. Hagen, Phase contrast micro-CT with adjustable in-slice spatial resolution at constant magnification, Phys. Med. Biol. **69**, 105017 (2024).

[23] M. Esposito, L. Massimi, I. Buchanan, J. D. Ferrara, M. Endrizzi, and A. Olivo, A laboratory-based, low-energy, multi-modal x-ray microscope with user-defined resolution, Appl. Phys. Lett. **120**, 234101 (2022).

[24] C. Shannon, Communication in the presence of noise, Proc. IRE **37**, 10 (1949).

[25] C. K. Hagen, F. A. Vittoria, O. Roche i Morgo, M. Endrizzi, and A. Olivo, Cycloidal computed tomography, Phys. Rev. Appl. **14**, 014069 (2020).

[26] W. Kalender, Principles and applications of spiral CT, Nucl. Med. Biol. **21**, 693 (1994).

[27] M. D. De Jonge, A. M. Kingston, N. Afshar, J. Garrevoet, R. Kirkham, G. Ruben, G. R. Myers, S. J. Latham, D. L. Howard, D. J. Paterson, C. J. Ryan, and G. McColl, Spiral scanning X-ray fluorescence computed tomography, Opt. Express **25**, 23424 (2017).

[28] D. J. Ching, M. Hidayetoglu, T. Bicer, and D. Gursoy, Rotation-as-fast-axis scanning-probe x-ray tomography: the importance of angular diversity, Appl. Opt. **57**, 8780 (2018).

[29] O. Roche i Morgo, F. A. Vittoria, M. Endrizzi, A. Olivo, and C. K. Hagen, Technical Note: Practical implementation strategies for cycloidal computed tomography, Med. Phys. **48**, 6524 (2021).

[30] G. Lioliou, O. Roche i Morgo, S. Marathe, K. Wanelik, S. Cipiccia, A. Olivo, and C. K. Hagen, Cycloidal-spiral sampling for three-modal x-ray CT flyscans with two-dimensional phase sensitivity, Sci. Rep. **12**, 21336 (2022).

[31] G. Lioliou, C. Navarrete-Leon, A. Astolfo, S. Savvidis, D. Bate, M. Endrizzi, C. K. Hagen, and A. Olivo, A laboratory-based beam tracking x-ray imaging method achieving two-dimensional phase sensitivity and isotropic resolution with unidirectional undersampling, Sci. Rep. **13**, 8707 (2023).

[32] F. Pfeiffer, T. Weitkamp, O. Bunk, and C. David, Phase retrieval and differential phase-contrast imaging with low-brilliance X-ray sources, Nat. Phys. **2**, 258 (2006).

[33] K. Morgan, D. Paganin, and K. Siu, X-ray phase imaging with a paper analyzer, Appl. Phys. Lett. **100**, 124102 (2012).

[34] P. Rattey and A. Lindgren, Sampling the 2-D Radon transform, IEEE. Trans. Acoust. Speech Signal Process. **29**, 994 (1981).

[35] C. K. Hagen, F. A. Vittoria, M. Endrizzi, and A. Olivo, Theoretical framework for spatial resolution in edge-illumination x-ray tomography, Phys. Rev. Appl. **10**, 054050 (2018).

[36] See Supplemental Material at http://link.aps.org/supplemental/10.1103/PhysRevApplied.22.034011 for a simulation study performed to confirm the optimality of the cycloidal sampling conditions for micro-CT systems with amplitude-modulated beams. References [20,42,43] are also cited in Supplemental Material.

[37] L. Massimi, *et al.*, in *Proc. SPIE 10948*, Medical Imaging 2019: Physics of Medical Imaging 109481R (SPIE, 2019).

[38] O. Roche i Morgo, J. Aleksejev, A. Astolfo, S. Savvidis, M. F. M. Gerli, S. Cipiccia, A. Olivo, and C. K. Hagen, Utility of knife-edge position tracking in cycloidal computed tomography, Opt. Express **30**, 43209 (2022).

[39] L. Feldkamp, L. David, and K. Kress, Practical cone-beam algorithm, J. Opt. Soc. Am. A **1**, 612 (1984).

[40] C. Romano, J. M. Minto, Z. K. Shipton, and R. J. Lunn, Automated high accuracy, rapid beam hardening correction in X-ray computed tomography of multi-mineral, heterogeneous core samples, Comput. Geosci. **131**, 144 (2019).

[41] S. Savvidis, M. F. M. Gerli, M. Pellegrini, L. Massimi, C. K. Hagen, M. Endrizzi, A. Atzeni, O. K. Ogunbiyi, M. Turmaine, E. S. Smith, C. Fagiani, G. Selmin, L. Urbani, N. Durkin, S. Shibuya, P. De Coppi, and A. Olivo, Monitoring tissue engineered constructs and protocols with laboratory-based x-ray phase contrast tomography, Acta Biomater. **141**, 290 (2022).

[42] F. A. Vittoria, P. C. Diemoz, M. Endrizzi, L. Rigon, F. C. Lopez, D. Dreossi, P. R. T. Munro, and A. Olivo, Strategies for efficient and fast wave optics simulation of coded-aperture and other x-ray phase-contrast imaging methods, Appl. Opt. **52**, 6940 (2013).

[43] D. Paganin, S. C. Mayo, T. E. Gureyev, P. R. Miller, and S. W. Wilkins, Simultaneous phase and amplitude extraction from a single defocused image of a homogeneous object, J. Microsc. **206**, 33 (2002).